

# Looking into the faintEst With MUSE (LEWIS): Exploring the nature of ultra-diffuse galaxies in the Hydra-I cluster

## VI. A star-forming UDG in Hydra I: a rare UDG or a transition phase?

Luca Rossi<sup>1,2</sup>, Chiara Buttitta<sup>1\*</sup>, Goran Doll<sup>1,2</sup>, Enrichetta Iodice<sup>1</sup>, Marco Gullieuszik<sup>3</sup>, Marc Sarzi<sup>4</sup>, Marco Mirabile<sup>5,6</sup>, Johanna Hartke<sup>7,8,9</sup>, Magda Arnaboldi<sup>10</sup>, Rosa Calvi<sup>1</sup>, Michele Cantiello<sup>11</sup>, Enrico Maria Corsini<sup>3,12</sup>, Giuseppe D'Ago<sup>13</sup>, Jesús Falcón-Barroso<sup>14,15</sup>, Francesca Fonzo<sup>1</sup>, Duncan A. Forbes<sup>16</sup>, Michael Hilker<sup>10</sup>, Antonio La Marca<sup>17,18</sup>, Alessandro Loni<sup>1</sup>, Steffen Mieske<sup>19</sup>, Maurizio Paolillo<sup>1,2</sup>, Marina Rejkuba<sup>10</sup>, Marilena Spavone<sup>1</sup>, and Chiara Spiniello<sup>10,20,1</sup>

(Affiliations can be found after the references)

Received MM DD, YYYY; accepted MM DD, YYYY

### ABSTRACT

**Context.** This paper presents a detailed analysis of a gas-rich star-forming ultra-diffuse galaxy (UDG) as part of the ESO Large Programme 'Looking into the faintEst With MUSE (LEWIS)'. Among the UDGs in the LEWIS sample, UDG 6 is the only galaxy that hosts a significant amount of ionised gas with evidence of emission lines, suggesting recent star-forming activity.

**Aims.** The main goal of this work is to constrain the formation history of this UDG by comparing its properties with the main formation scenarios proposed for this extreme class of galaxies.

**Methods.** We adopted integral field spectroscopy from MUSE to derive the morphology and the structural properties of the stellar and gas components of UDG 6. We applied spectral fitting and Voronoi tessellation algorithms to the MUSE data-cube to derive the kinematics and properties of the gas and stellar component, explore gas dynamics, and characterise emission lines. Moreover, we derived the GCs populations' properties by applying a multi-band spectrophotometric analysis.

**Results.** We confirmed that UDG 6 is a member of Hydra I cluster with a systemic velocity of  $V_{\text{sys,*}} \sim 3580 \text{ km s}^{-1}$ . It is characterised by a regular and elongated shape and contains a significant dust content ( $A_V = 1.2 \pm 0.5 \text{ mag}$ ), a metal-poor ( $12 + \log_{10}(\text{O}/\text{H}) = 7.7 \pm 0.2 \text{ dex}$ ) ionised gas fraction ( $f_{\text{gas}} = 0.24 \pm 0.08$ ) and an underlying old-to-intermediate ( $\geq 3 \text{ Gyr}$ ) stellar component. Evidence of local and clumpy star-forming activity has been revealed through the analysis of emission line ratios, and an arc-like tidal feature was discovered from unsharp masking analysis. The number counts of GCs in UDG 6 is  $N_{\text{GC}} = 0.2 \pm 5.4$ .

**Conclusions.** Like the other UDGs in LEWIS, UDG 6 might originate from a 'puffed-up dwarf' whose stellar content has been stretched out to larger radii, passively evolving into a more diffuse galaxy. Being located in a dynamically active region of the cluster, characterised by tidal features and stripping phenomena, we suggest that the environmental processes have played a role in shaping the properties of UDG 6. A tidal interaction with a nearby galaxy might have triggered recent star-formation activity, without dramatically altering the coherent gas rotation in UDG 6.

**Key words.** Galaxies: individual: UDG 6 - Galaxies: photometry - Galaxies: kinematics and dynamics - Galaxies: structure - Galaxies: formation - Galaxies: evolution

## 1. Introduction

Ultra-diffuse galaxies are low-mass ( $M_* \sim 10^{5-9} M_{\odot}$ ) galaxies empirically defined to have a central surface brightness of  $\mu_{0,g} > 24 \text{ mag arcsec}^{-2}$  and effective radius of  $R_{\text{eff}} > 1.5 \text{ kpc}$  (van Dokkum et al. 2015). They are generally considered to represent the extreme low-surface-brightness (LSB) extension of the dwarf galaxy population.

Large populations of UDGs have been mainly identified and studied in dense environments such as clusters of galaxies and groups, where the majority of deep and wide optical imaging surveys focused (van der Burg et al. 2016; Román & Trujillo 2017; Spekkens & Karunakaran 2018; Mancera Piña et al. 2019; Iodice et al. 2020; Lim et al. 2020; Kado-Fong et al. 2022; La Marca et al. 2022a; Zaritsky et al. 2023; Marleau et al. 2025; Makda et al. 2025). UDGs in moderate-to-low density environments, such as filaments and isolated fields, have also been detected via HI surveys (Trujillo et al. 2017; Leisman et al. 2017;

Mancera Piña et al. 2020; Janowiecki et al. 2019; Karunakaran et al. 2020; Adams et al. 2026). The dataset of UDGs collected so far allows us to identify several classes of UDGs with distinct properties suggesting different formation channels (see Gannon et al. 2026, for a review).

UDGs in dense environments are typically red, quenched, and gas-poor. Their metallicity, globular clusters (GCs), and dark matter (DM) content span wide ranges of values, which correlate with the environment where they reside and the physical mechanisms they underwent in the past (Gannon et al. 2022; Ferré-Mateu et al. 2023; Buzzo et al. 2024; Buttitta et al. 2025; Doll et al. 2026). UDGs located in groups, in clusters' outskirts or in fields, are instead bluer and star-forming, dusty and gas-rich, with an irregular shape and extended and coherent velocity fields (Prole et al. 2019; Mancera Piña et al. 2020; Gault et al. 2021).

Despite the existence of multiple classes of UDGs being largely accepted by the scientific community, the present-day picture of the UDG framework remains mostly unclear because the current dataset of UDGs in different environments is un-

\* e-mail: chiara.buttitta@inaf.it

balanced. While deep optical imaging surveys have identified thousands of UDG candidates by detecting their stellar component (e.g. Zaritsky & Behroozi 2023), their neutral or ionised gas counterpart has been revealed only for a small number of UDGs (see e.g. Kadowaki et al. 2017; Leisman et al. 2017; Papastergis et al. 2017; Janowiecki et al. 2019). Therefore, it remains unclear whether the observed environmental differences between UDG populations reflect a genuine physical process or are partly driven by observational selection effects. Cluster UDGs could be the last evolutionary stage of the same type of objects located outside the clusters (Román & Trujillo 2017). Once they enter dense environments, mechanisms such as ram-pressure stripping, tidal interactions, and galaxy harassment can efficiently remove gas from galaxies, potentially transforming gas-rich, star-forming UDGs into quiescent ones (Venholá et al. 2017; Wittmann et al. 2017; Safarzadeh & Scannapieco 2017; Mancera Piña et al. 2018; Sales et al. 2020).

Spectroscopic observations are fundamental to fill the gap between stellar and gas counterpart statistics. By probing the kinematics, gas content, and emission lines, spectroscopy provides direct insight into ongoing star formation, stellar populations, and the impact of environmental mechanisms. These quantities are key parameters for testing how different formation channels produce inherently distinct UDGs populations. In this context, the ‘Looking into the faintest With MUSE’ (LEWIS) project provided a precious contribution to improving our understanding of UDGs (Iodice et al. 2023). Combining deep optical data from VST and integral-field (IF) from the MUSE spectrograph, LEWIS revealed the existence of multiple classes of UDG population in a single environment, characterised by different properties (Buttitta et al. 2025; Doll et al. 2026).

In this paper, we present a detailed analysis of UDG 6, a rare example of a gas-rich UDG in Hydra, as evidenced by clear emission lines from ionised gas. The paper is organised as follows. In Section 2 we describe the structural properties and morphology of UDG 6 and describe the spectroscopic data used throughout this work. In Section 3, we show the morphological analysis performed on the MUSE reconstructed images. In Section 4, we discuss the spectroscopic analysis performed on the MUSE data-cube to derive properties of stellar and gas components in UDG 6. In Section 5, we discuss the physical implications of the obtained results within the environment and in the LEWIS sample framework. Finally, in Section 6, we report our conclusions and future perspectives. Throughout the paper, we adopt the standard  $\Lambda$ CDM cosmology (Hinshaw et al. 2013):  $H_0 = 70 \text{ km s}^{-1} \text{ Mpc}^{-1}$ ,  $\Omega_m = 0.3$ , and  $\Omega_\Lambda = 0.7$ .

## 2. Observations

### 2.1. Properties of UDG 6 from deep imaging

UDG 6 was originally identified in the VST Early-type Galaxy Survey (VEGAS<sup>1</sup>, Capaccioli et al. 2015; Iodice et al. 2021) performed at the European Southern Observatory (ESO) VLT Survey Telescope (VST). VEGAS is a deep multi-band imaging survey of nearby ( $z < 0.05$ ) groups and clusters of galaxies, to map the light distribution down to a surface brightness level of  $\mu_g \sim 27 - 28 \text{ mag arcsec}^{-2}$  in  $g$  band.

UDG 6 is located in the Hydra I cluster of galaxies, a dense environment of galaxies at a distance  $D \sim 51 \text{ Mpc}$  (Christlein & Zabludoff 2003) which shows signs of ongoing interactions and mass assembly around the dominant central cluster galaxy

Table 1: Structural properties of UDG 6.

	Property		UDG 6
(1)	RA	[J2000]	+10h 36m 35.80s
(2)	Dec	[J2000]	-27d 19m 36.12s
(3)	$M_r$	[mag]	-14.38 $\pm$ 0.08
(4)	$g - r$	[mag]	0.32 $\pm$ 0.20
(5)	$\mu_0$	[mag arcsec <sup>-2</sup> ]	24.08 $\pm$ 0.13
(6)	$R_{\text{eff}}$	[kpc]	1.37 $\pm$ 0.12
(7)	$M/L$	[ $M_\odot/L_\odot$ ]	0.70
(8)	$M_*$	[ $10^8 M_\odot$ ]	0.32

**Notes.** Galaxy properties of UDG 6 from Iodice et al. (2020). (1-2): the Right Ascension and Declination of the galaxy. (3): absolute magnitude in the  $r$  band. (4): average  $g - r$  colour. (5-6): central surface brightness and effective radius, respectively. (7-8): stellar mass-to-light ratio and stellar mass derived from  $r$  band, respectively.

NGC3311 (Arnaboldi et al. 2012; Spavone et al. 2024; Hess et al. 2022), and it belongs to the first sample of UDGs discovered in Hydra I (Iodice et al. 2020). UDG 6 is located at a projected cluster-centric distance of 12.2 arcmin from the cluster centre<sup>2</sup>, corresponding to a projected physical distance of  $\sim 180 \text{ kpc}$  and belongs to the north group of galaxies in Hydra I (Fig. 1, left panel). UDG 6 is in proximity to the lenticular galaxy HCC 005, which shows two prominent tidal tails, signs of the presence of tidal interactions acting on the galaxy (La Marca et al. 2022b; Spavone et al. 2024). The morphology of UDG 6 is regular, characterised by an elongated spheroidal shape (Fig. 1, right panel). Among the UDGs in Hydra I (Iodice et al. 2020; La Marca et al. 2022b), UDG 6 is one of the bluest ( $g - r = 0.32 \text{ mag}$ ) and least massive ( $M_* = 3.2 \cdot 10^7 M_\odot$ ) of the sample. The stellar mass estimate has been obtained from photometric analysis, by using the galaxy’s absolute magnitude, colour, and the relation presented in Into & Portinari (2013). Being very blue, the stellar mass could be a lower limit. We used deep  $H$ -band data from VIRCAM@VISTA telescope (Prog. ID. 109.231E.00, P.I. M. Cantiello) to derive an independent estimate of the stellar mass, and we obtained a value of  $M_* = (1.8 \pm 0.72) \cdot 10^7 M_\odot$ , consistent with the previous estimate within  $2\sigma$ . Finally, UDG 6 does not seem to have any GC candidates (Iodice et al. 2020). In Table 1, we report the structural parameters for UDG 6.

### 2.2. Spectroscopic data from LEWIS

Spectroscopic data of UDG 6 were acquired under the LEWIS<sup>3</sup> project (Prog. ID. 108.222P, P.I. E. Iodice), whose observations were carried out at the ESO Multi Unit Spectroscopic Explorer (MUSE, Bacon et al. 2010). Configured in wide-field mode, MUSE offers a field-of-view (FOV) of  $1 \times 1 \text{ arcmin}^2$  with a spatial sampling of  $0.2 \text{ arcsec pixel}^{-1}$ . The MUSE nominal wavelength range is  $4800 - 9300 \text{ \AA}$ , with a spectral sampling of  $1.25 \text{ \AA pixel}^{-1}$  and an average spectral resolution of  $\text{FWHM} = 2.51 \text{ \AA}$  (Bacon et al. 2017). The spectral resolution of the LEWIS data was derived in Buttitta et al. 2025 (hereafter Paper II). It varies from  $\text{FWHM} = 2.75 \text{ \AA}$  ( $\sigma \sim 70 \text{ km s}^{-1}$ ) at  $\lambda \sim 5000 \text{ \AA}$  to  $\text{FWHM} = 2.63 \text{ \AA}$  ( $\sigma \sim 37 \text{ km s}^{-1}$ ) at  $\lambda \sim 9000 \text{ \AA}$ .

<sup>2</sup> We assumed as cluster centre the coordinates of the bright cluster member NGC3311 (RA = 159.17842°, Dec = -27.528339°) as done in previous works (Forbes et al. 2023; Buttitta et al. 2025).

<sup>3</sup> for details, see <https://sites.google.com/inaf.it/lewis/home>

<sup>1</sup> for details, see <https://sites.google.com/inaf.it/vegas/home>

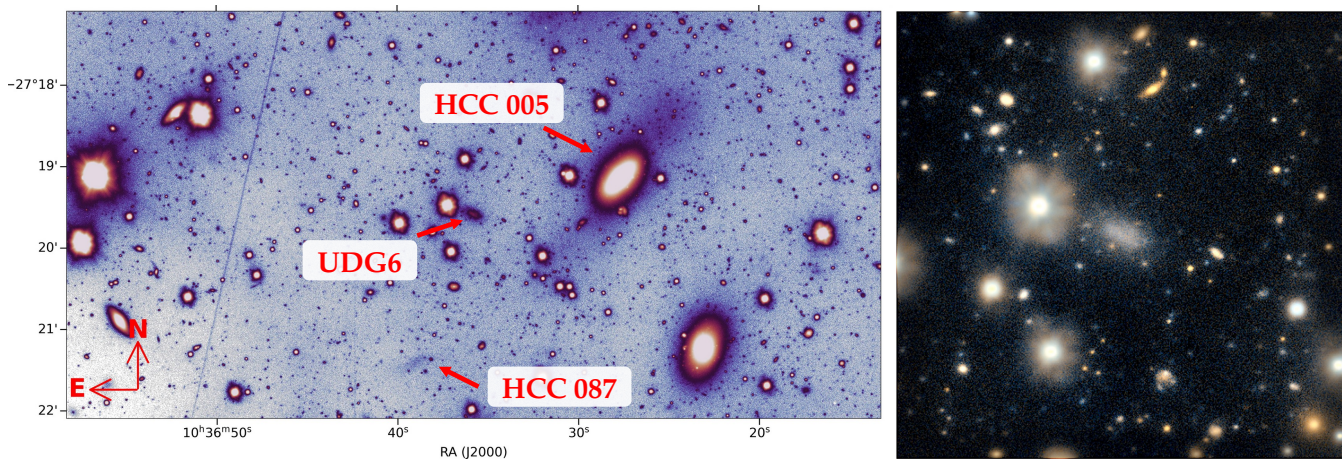


Fig. 1: OmegaCAM@VST  $r$ -band image of the North group of the Hydra I cluster, adapted from ESO/INAF/M. Spavone, E. Iodice. Left panel: The field-of-view is  $10 \times 5$  arcmin<sup>2</sup>. Right panel: Zoom-in  $g - r$  colour-composite image of UDG 6. The field-of-view is  $1.6 \times 1.6$  arcmin<sup>2</sup>

Data of UDG 6 were acquired on three different observation blocks (OB): 23 – 24 April 2023, 18 – 19 December 2023, and 12 – 13 January 2024. Within each OB, three exposures, with an integration time of 900 seconds for each, were obtained. The total exposure time on target is 2.25 hours, with an average seeing of FWHM  $\sim 1.09$  arcsec. A standard data reduction was performed using the MUSE pipeline (Weilbacher et al. 2020) running on the ESOREFLEX workflow (Freudling et al. 2013). As for other galaxies in LEWIS, we used the previous result to perform a second improved data reduction, following the procedures described in Paper II, to improve the data quality and reduce sky-background fluctuations. MUSE data have been used to perform a detailed analysis of the galaxy’s morphology and properties.

### 3. Morphology of UDG 6

#### 3.1. Isophotal analysis

We recovered the mean geometric parameters of UDG 6 by performing an isophotal analysis on the reconstructed MUSE white image (Fig. 2, left panel) using the ELLIPSE task of the Python package PHOTUTILS (Bradley et al. 2023). This type of analysis has already been carried out on deep VST imaging data (Iodice et al. 2020). However, we will take advantage of the wider spectral coverage of MUSE to capture the light contribution of both stellar and gas components in UDG 6.

We followed the prescription described in Paper II: we masked all the foreground stars, background galaxies, and spurious sources in the FOV, then we performed a first isophotal fit to determine the centre of the galaxy. Therefore, we allowed the centre coordinates of the ellipses free to vary and fixed the values of position angle (PA) and ellipticity ( $\epsilon$ ) to the values obtained from the isophotal analysis performed on VST images. We iteratively computed the mean and standard deviation of centre coordinates values of fitted isophotes to identify the radial convergence interval, i.e. the radial range where  $\langle x \rangle$  and  $\langle y \rangle$  reach stability within  $\sigma_x$  and  $\sigma_y$ , respectively. The values of  $\langle x \rangle$  and  $\langle y \rangle$  computed in the radial region FWHM  $< a \lesssim 0.3 R_{\text{eff}}$ , with  $a$  semi-major axis of the fitted isophote and  $R_{\text{eff}}$  effective radius (Iodice et al. 2020), determined the galaxy centre  $(x_c, y_c)$ . This preliminary analysis revealed a shift in the centre coordinate, with respect to the previously estimate, towards the eastern

direction of  $\Delta x \sim 1$  arcsec beyond  $\gtrsim 0.4 R_{\text{eff}}$ , probably due to a possible light contamination from the nearby bright star.

We performed a second fit of the galaxy isophotes by fixing the centre coordinates previously defined and letting the  $\epsilon$  and PA of the isophotes free to vary. By inspecting the radial profiles of the fitted isophote parameters (Fig. 2, bottom panels), we found that the orientation of the fitted isophotes remains nearly constant, while the ellipses become more elongated with increasing radial distance, reaching a peak of  $\epsilon \sim 0.7$  at  $a \sim 0.5 R_{\text{eff}}$  and becoming more roundish again at  $a \sim 1 R_{\text{eff}}$ . We obtained the geometric parameters of the galaxy by computing the average values of the PA and  $\epsilon$  of the best-fitted isophotes in the radial range between the FWHM of the PSF ( $\sim 0.2 R_{\text{eff}}$ ) and the largest radius where the isophotes best-fit is reliable ( $\sim 1.1 R_{\text{eff}}$ ). We therefore obtained  $\langle \epsilon \rangle = 0.6$  and  $\langle \text{PA} \rangle = 65^\circ$ , consistent with the values obtained from isophotal analysis performed on VST images (Iodice et al. 2020). We used these parameters  $(x_c, y_c, \langle \epsilon \rangle, \langle \text{PA} \rangle, R_{\text{eff}})$  to define the elliptical aperture within which we co-added all the spaxels and derived the stacked spectrum, which was then used to perform the integrated spectral analysis of UDG 6.

#### 3.2. Unsharp mask

The isophotal analysis revealed a regular morphology in UDG 6, characterised by elongated isophotes with constant orientation on the sky plane. However, this type of analysis can give us hints only on the global symmetry and large-scale structures of the galaxy. Therefore, we decided to perform an unsharp mask analysis on the MUSE reconstructed image to investigate the presence of small-scale features and sub-structures that could be hidden by the diffuse light distribution of UDG 6. For this reason, we convolved the image with Gaussian kernels of different sizes in units of the MUSE FWHM in the range 2-14 FWHM to maximise the light contrast of possible features. Fig. 3, shows the unsharp mask on the white image of UDG 6 obtained from the best kernel size ( $\sigma_{\text{kernel}} = 8$  FWHMs). We applied the same analysis on two additional images, obtained by collapsing the data-cube in the bluest ( $4800 < \lambda < 7000 \text{ \AA}$ , Fig. 3, central panel) and in the reddest ( $7000 < \lambda < 9200 \text{ \AA}$ , Fig. 3, right panel) spectral range. The two ranges were chosen to split the spectral region where emission lines were visible, from the longer wavelength, more contaminated and without emissions. This multi-band ap-

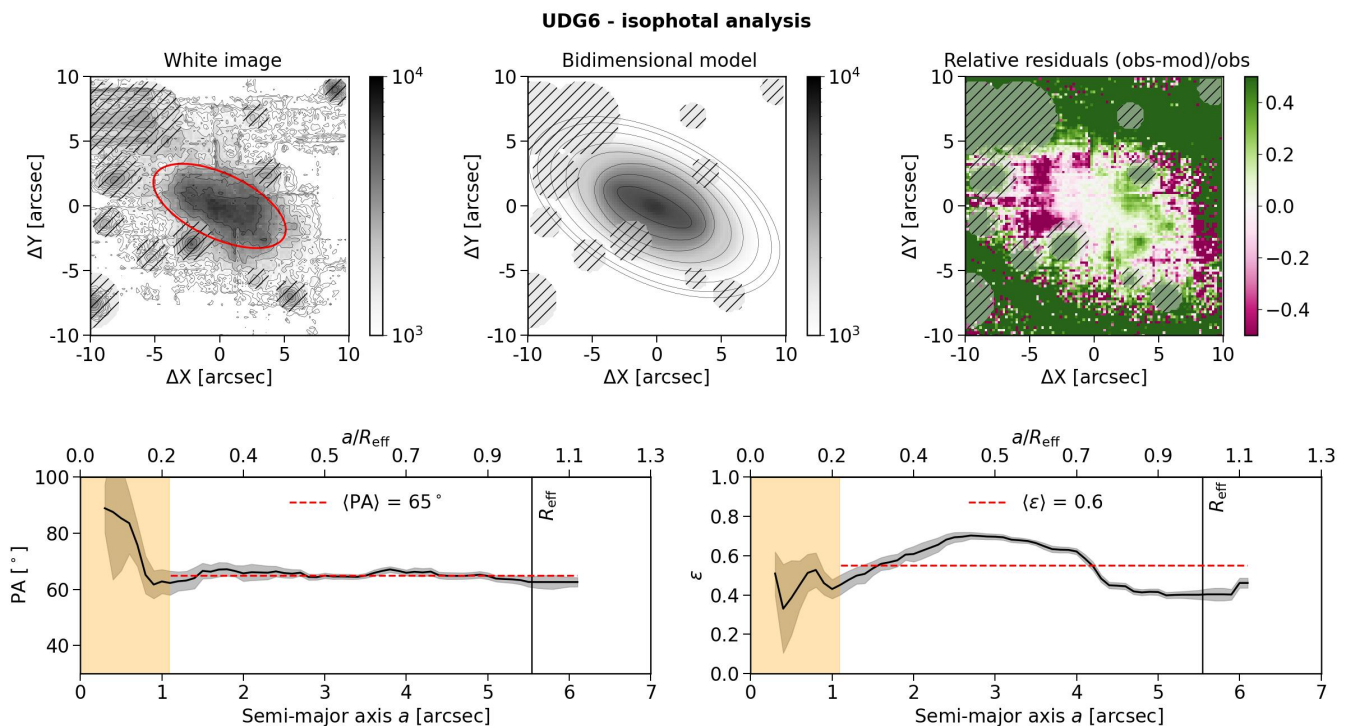


Fig. 2: Isophotal analysis of UDG 6. Top panels: MUSE reconstructed white image of UDG 6 with contours (left), bi-dimensional model from isophotal fitting (centre), and relative residuals (right). The grey hatched circles represent the masked regions. The red ellipse represents the position of  $R_{\text{eff}}$  and marks the region used to extract the stacked spectrum. Bottom panels: Radial profiles of PA (left) and  $\epsilon$  (right) of fitted isophotes (solid lines) with  $1\sigma$  uncertainties (grey shaded regions). The orange shaded region marks the PSF-limited region. The mean geometric parameters of the galaxy are marked by red dashed lines. The vertical black line marks the position of  $R_{\text{eff}}$ .

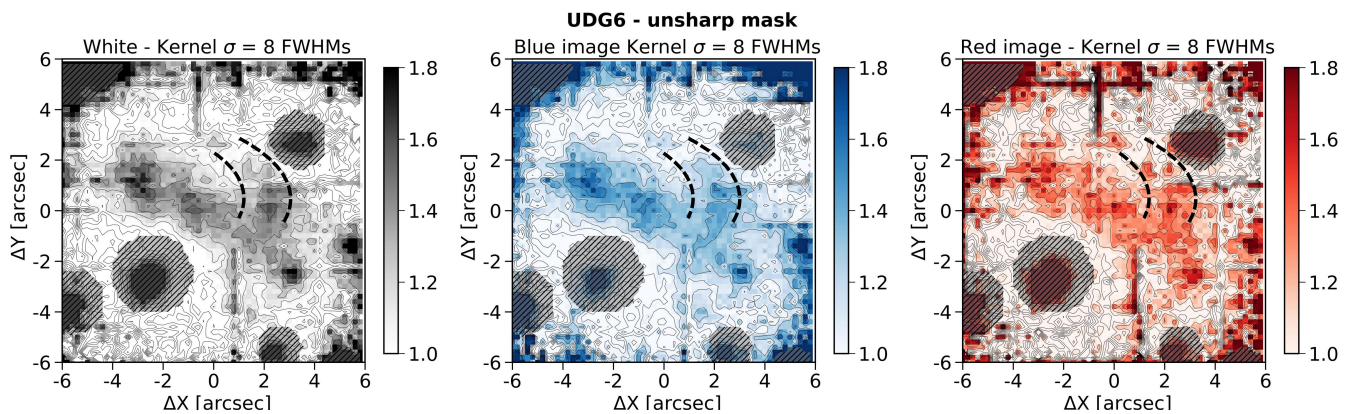


Fig. 3: Unsharp mask of UDG 6. Total white image ( $4800 < \lambda < 9200 \text{ \AA}$ , left), blue image ( $4800 < \lambda < 7000 \text{ \AA}$ , centre), and red image ( $7000 < \lambda < 9200 \text{ \AA}$ , right) obtained by collapsing the MUSE data-cube along the spectral direction. The adopted Gaussian kernel size is  $\sigma_{\text{kernel}} = 8$  FWHMs. Grey hatched circles represent the masked regions, while the black dashed line delimits the spiral-like feature.

proach aims to reveal not only the various coherent structures that constitute the galaxy, but also assess the relative light contribution of the different components dominant in certain spectral ranges.

In both the unsharp-masked white-light and blue-band images of UDG 6, a distinct arc or spiral-like feature is visible, extending from the right side of the galaxy’s main elongated body and curving towards the north-east (see Fig. 3). The feature is less evident in the red image, which appears clumpier and disturbed. The red image also appears noisier since the redder spec-

tral range of the MUSE data-cube contains several sky-line residual features. Since the blue image ( $\lambda < 7000 \text{ \AA}$ ) contains prominent gas emission lines (see Section 4.1), we can reasonably assume that the arc-like feature is associated with these strong emissions rather than the underlying stellar continuum (see also Section 4). These findings suggest a possible gravitational interaction or distortion on UDG 6 due to the proximity of nearby lenticular galaxy HCC 005 (Fig. 1, left panel). We will present a more detailed discussion of this hypothesis in Section 5.

## 4. Spectroscopic analysis

In this section, we describe the spectroscopic analysis performed on UDG 6. We recovered the integrated global properties (1D) such as kinematics (Section 4.1) and properties of stars (Section 4.2), and gas (Sections 4.3 and 4.4), as well as, taking advantage of the IF nature of LEWIS data, spatially-resolved (2D) gas kinematics maps (Section 4.5).

### 4.1. Integrated stellar and gas kinematics

The main peculiarity of UDG 6 resides in the presence of strong emission lines (Fig. 4, top panel). Among the galaxies in LEWIS (Iodice et al. 2023), UDG 6 is the only UDG which shows prominent emission lines, such as Balmer lines  $H\beta$  ( $\lambda 4861 \text{ \AA}$ ) and  $H\alpha$  ( $\lambda 6563 \text{ \AA}$ ), the [O III] doublet ( $\lambda\lambda 4959, 5007 \text{ \AA}$ ), the reddest line of the [N II] doublet ( $\lambda\lambda 6548, 6583 \text{ \AA}$ )<sup>4</sup> and the [S II] doublet ( $\lambda\lambda 6716, 6731 \text{ \AA}$ ). While other UDGs in LEWIS show clear absorption features such as  $H\beta$  and  $H\alpha$ , magnesium (Mg I,  $\lambda\lambda 5167, 5173, 5184 \text{ \AA}$ ) and the calcium (CaT,  $\lambda\lambda 8498, 8542, 8662 \text{ \AA}$ ) triplets and iron absorption lines (Fe I,  $\lambda\lambda 5198.71, 5270.40, 5335.16 \text{ \AA}$ ), the spectrum of UDG 6 only shows extremely weak stellar absorption features. The spectral profile of  $H\beta$  shows hints of a broad absorption line with emission on top (Fig. 4, bottom left panel). A few extremely weak iron absorption lines are also present in the spectrum, while the Mg I triplet is barely visible (Fig. 4, bottom central panel). At wavelengths longer than  $\sim 7000 \text{ \AA}$ , the spectrum is strongly affected by residuals from sky emission lines, with the calcium triplet region (CaT;  $\lambda \sim 8500\text{-}8800 \text{ \AA}$ ) being particularly noisy and heavily contaminated. We carefully inspected this region, and the effect of the Zurich Atmosphere Purge algorithm (ZAP, Soto et al. 2016), realizing that ZAP creates a fictitious absorption-line CaT (see Paper II for a description of the adopted ZAP recipe). Therefore, we decided to focus our analysis on the optical spectral range up to  $7000 \text{ \AA}$ , which has an average FWHM  $\sim 2.69 \text{ \AA}$  corresponding to  $\sigma \approx 49 \text{ km s}^{-1}$ .

Following the same approach presented in Paper I and Paper II, we performed spectral fitting on the stacked spectrum obtained from an elliptical aperture with geometric parameters derived from the isophotal analysis (see Section 2). We used the pPXF algorithm (Cappellari & Emsellem 2004; Cappellari 2017, 2023) to derive the line-of-sight (LOS) velocity distribution (LOSVD) of both stars and gas in UDG 6. The LOSVD is commonly parametrised via the LOS velocity ( $V_{\text{LOS}}$ ), velocity dispersion ( $\sigma_{\text{LOS}}$ ), and Gaussian-Hermite moments  $h_3$  and  $h_4$  (Gerhard 1993; van der Marel & Franx 1993). However, given the LSB nature of UDGs and the limitations in the quality of the spectroscopic data ( $S/N \sim 20$ ), we can constrain, at most, the first two moments of the LOSVD, focusing on the optical spectral range ( $4800\text{-}7000 \text{ \AA}$ ). In addition, since Balmer lines are clearly visible in the spectrum, we fitted the reddening (see Cappellari 2023, for a description).

We account for three components with a different LOSVD: one for the stars and two for the gas, the Balmer and the forbidden gas emission lines. For the stellar component, we adopted the E-MILES single stellar population (SSP) models (Vazdekis et al. 2012, 2016), based on Padova isochrones (Girardi, L. et al. 2000) and a Kroupa (Kroupa 2001) initial-mass function. The E-MILES SSPs have a spectral resolution of  $\text{FWHM} = 2.51 \text{ \AA}$ , and cover a wide spectral ( $1680 - 50000 \text{ \AA}$ ),

metallicity ( $-2.27 \leq [M/H] \leq +0.04$ ), and age ( $30 \text{ Myr} \leq \text{age} \leq 14 \text{ Gyr}$ ) ranges. For the emission lines, we adopted four gas spectral templates, one for the Balmer lines ( $H\alpha$  and  $H\beta$ ), fixing their ratio to the Balmer decrement, and the other three for the emission lines ([O III], [N II], and [S II] doublets). The amplitude ratios of the emission lines are constrained by intrinsic theoretical decrements, assuming no dust extinction ( $H\alpha/H\beta = 2.86$ ,  $[S II]\lambda 6716/[S II]\lambda 6731 \in [0.44, 1.43]$ ,  $[N II]\lambda 6548/[N II]\lambda 6583 = 0.33$ ,  $[O III]\lambda 4959/[O III]\lambda 5007 = 0.33$ , Osterbrock & Ferland 2006). As described in Paper II, we used the MUSE line-spread function (LSF) of LEWIS data and adopted both multiplicative – to correct the continuum shape for possible flux calibration imperfections in the spectrum – and additive – to correct the mismatch between the stellar templates and the spectral continuum – Legendre polynomials. We tested different values of the polynomial degrees in the range  $[0, 12]$  with a step of 2, and evaluated the quality of the best-fit from the  $\chi^2$  value. The best fit is obtained with both additive and multiplicative polynomials of degree 4.

The uncertainties on the fitted parameters have been derived using Monte Carlo simulations and following the same procedure as described in Paper II. We generated 500 perturbations of the original spectrum by randomly adding Poissonian noise and removing/replacing portions of masked spectral regions, without altering the final S/N of the perturbed spectra. The errors on  $V_{\text{LOS}}$  and  $\sigma_{\text{LOS}}$  are derived as the standard deviations of the distributions of the fitted kinematic parameters.

In Fig. 4, we show the 1D stacked spectrum of UDG 6 with its best-fit from pPXF. From the best-fit of the gas component (yellow lines), we obtained a value of  $V_{\text{LOS, gas}} = 3559 \pm 1 \text{ km s}^{-1}$  for all emission lines. We obtained values of  $\sigma_{\text{LOS}}$  consistent within  $1\sigma$  as well ( $\sigma_{\text{LOS, Balmer}} = 18 \pm 1 \text{ km s}^{-1}$  and  $\sigma_{\text{LOS, forbidden}} = 22 \pm 4 \text{ km s}^{-1}$ ). The spectral fit of the stellar component is instead poor. This is mainly due to the absence of prominent absorption lines in the spectrum rather than the quality of the spectrum ( $S/N \sim 20$ ). The spectral fit returned an exceptionally high value of  $\sigma_{\text{LOS, *}}$ , resulting in an artificial broadening of the best-fit profile (red line). Thus we can only rely on the fitted line-of-sight velocity, which is  $V_{\text{LOS, *}} = 3584 \pm 15 \text{ km s}^{-1}$ . This value is consistent within  $2\sigma$  with the estimate obtained for the gas component.

### 4.2. Age and metallicity of stars

We used the spectral fitting algorithm pPXF to derive the integrated stellar population properties of UDG 6, following a similar approach as described in Doll et al. (2026) (hereafter Paper V), fitting the spectrum in the range  $4800 - 5500 \text{ \AA}$ , adopting E-MILES stellar templates and a regularisation factor of 50 (see Paper V for a description). Since the value of velocity dispersion for the stellar component is unreliable, we extrapolate the  $\sigma_{\text{eff}}$  from the Faber-Jackson relation for dwarf galaxies (Kirby et al. 2013,  $\sigma_{\text{eff, FJ}} = 19 \text{ km s}^{-1}$ ), consistent with the  $\sigma_{\text{LOS, gas}}$ . Given the extremely weak absorption features, the spectral fit is largely driven by the continuum shape, which can be significantly influenced by the adopted degree of the Legendre polynomials and by errors in the flux calibration. It is therefore essential to carefully assess the impact of the polynomial choice on the resulting fit. To this aim, we tested the effect of different multiplicative degrees exploring values in the same range adopted for the kinematics. In Fig. 5, we show the distributions of the stellar population light weights for three representative cases: 0, which corresponds to the case of a constant multiplicative polynomial, 4, the same as

<sup>4</sup> the bluest one, which is always fainter, is just barely detectable.

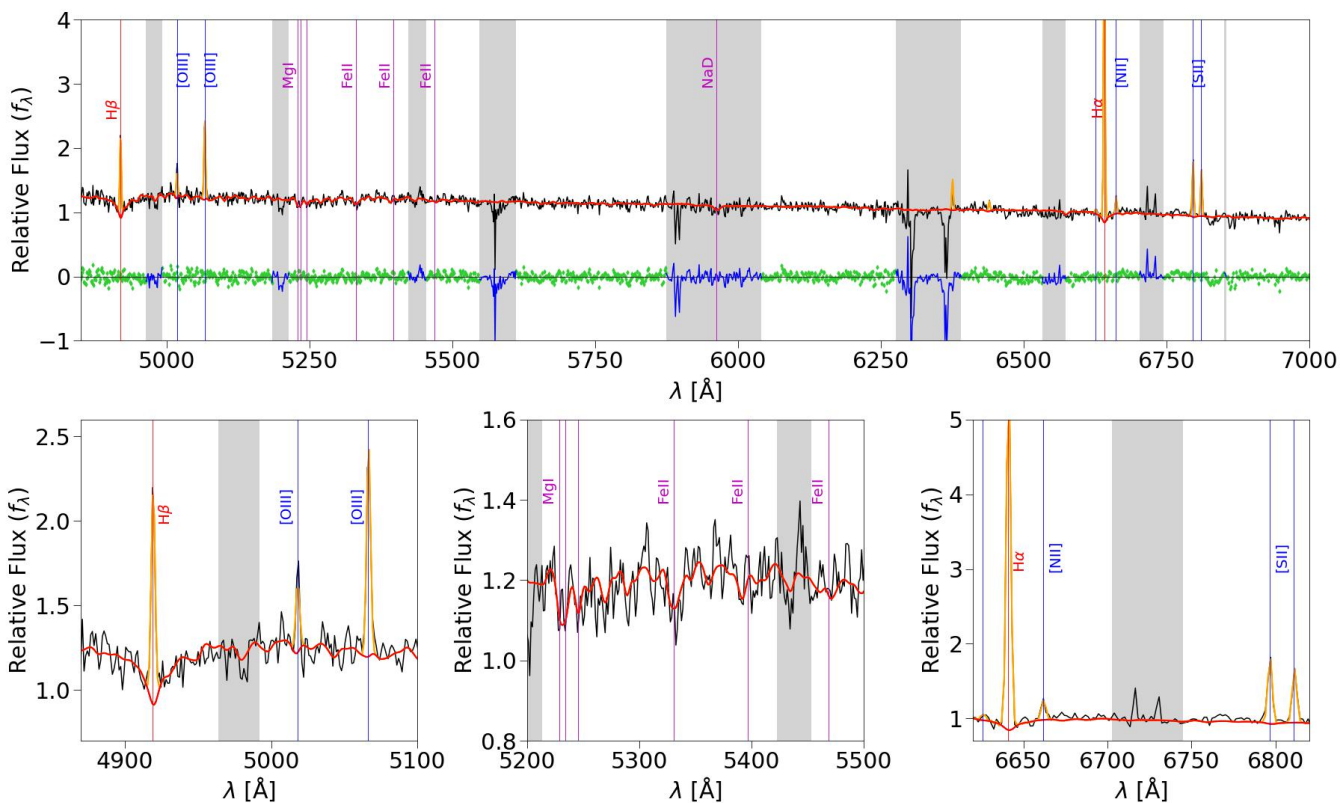


Fig. 4: Stacked spectrum of UDG 6 with its best-fit. Top row: the stacked spectrum is shown as a black line, and the best-fit obtained with `pPXF` is shown as a red solid line for the stellar component and in yellow for the gas components. The main absorption lines are marked in magenta, the Balmer emission lines in red, and the forbidden ones in blue, respectively. The residuals between the observed spectrum and the best-fit are shown as green points. The grey areas are the masked spectral regions of the spectra and are excluded from the fit. Bottom row: enlarged regions around the main fitted absorption and emission lines of the top-row fit.

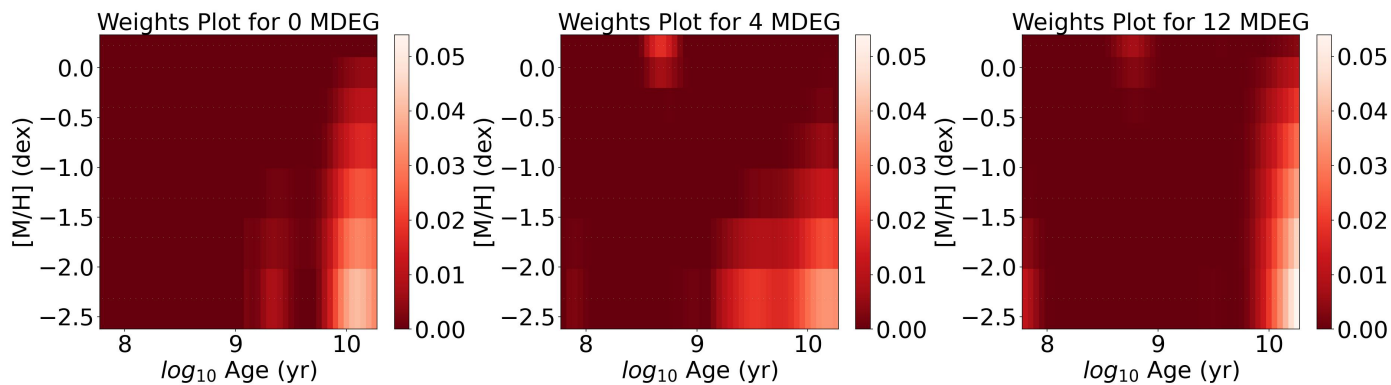


Fig. 5: Stellar population analysis of 1D stacked spectrum of UDG 6. Each panel shows the distributions of the stellar population light weights in the age-metallicity space for a spectral fit with multiplicative polynomials of degree equal to 0 (left), 4 (centre), and 12 (right).

the best-fit for kinematics, and 12, the largest value of the explored grid.

We noticed a significant fraction of weights located at age  $\gtrsim 3$  Gyr with metallicity spanning in the range  $[-2.5, -1]$  dex, independently from the choice of the tested polynomial degree. However, the spectral fit does not allow to fully constrain the metallicity. A minor contribution of younger stellar populations ( $< 10^8$  yr) is also present, but the weights that represent it are variable and negligible compared to the older population both in terms of mass and of light contribution. This younger population

could be responsible for the presence of strong emission lines in the spectrum of UDG 6. The best-fit with high polynomial degrees shows a consistent fraction of weights with nearly solar metallicity with an Age  $\sim 3 \cdot 10^8 - 10^9$  yr, which could be associated with the broad absorption line of  $H\beta$ . To test our hypothesis, we masked this broad absorption feature and repeated the spectral fitting, adopting the same configuration of `pPXF` and confirming that the solar-like metallicity contribution disappeared. We additionally repeated the spectral fit by fixing the mean metallicity to different values in the range  $[M/H] \in [0, -2]$  dex

with a step of 0.5, covering the possible values of the MILES stellar templates and investigating the quality of the resulting best-fit. However, all the fits share similar quality ( $\Delta\chi^2 \sim 0.01$ ). For the other multiplicative degree values explored in the range [2,12], the configurations of weights are similar to the 4 and 12 degree cases. We obtained similar results – a persistent old-to-intermediate contribution and variable younger contributions for multiplicative degrees larger than 0 – also for no regularization and for a regularization factor of 100. We performed an additional test based on the predictions of Blakeslee et al. (2001) and Vazdekis et al. (1996), which relate stellar population age and metallicity to broadband colours. We constrained the colour within its uncertainty range ( $g-r = 0.32 \pm 0.20$  mag) and required the stellar population age to be older than 3 Gyr. Nevertheless, the compatible models encompass a broad range of metallicities, preventing a robust constraint on this parameter. We concluded that UDG 6 contains a stellar component with an age of at least  $\geq 3$  Gyr, but its metallicity cannot be constrained by spectral fitting.

### 4.3. Star-forming regions

We investigated the nature of the ionisation source of the emission lines in UDG 6, measuring specific emission lines ratios and building the Baldwin, Phillips, & Terlevich (1981) diagram (hereafter BPT). We identified the strongest lines in the galaxy spectrum -  $H\beta$ , the [O III] doublet,  $H\alpha$ , and the [S II] doublet - and we constructed pseudo-narrow band images centred on these lines following the prescription presented in Hartke et al. (2025). In the following, we summarise the procedure: we extracted 50-pixel-wide band images centred on each emission line from the MUSE data-cube. The continuum was estimated from two 20-pixel-wide regions bracketing each line by computing the median flux, which was then subtracted to produce continuum-subtracted emission-line maps. In Fig. 6, we show the maps of Balmer (left panel) and forbidden (right panel) emission lines. Contours of  $H\alpha$  and  $H\beta$  are shown in red and blue, while those of [O III] and [S II] are shown in yellow and green, respectively.

The  $H\alpha$  and [S II] are widely distributed across the whole galaxy; in particular, the  $H\alpha$  is the most abundant component. Its distribution presents multiple peaks and shows an extension in the north-east part of the galaxy. The distributions of [O III] and  $H\beta$  are instead more clumpy and patchy. We do not show the map for the emission line of the [N II] since it is too faint, though it was detected in the galaxy's stacked spectrum.

We corrected the flux of the emission lines for the Milky Way Galaxy extinction (Fitzpatrick & Massa 2007), adopting as interstellar extinction and colour excess the values for the Milky Way ( $A_V = 0.217$  mag and  $A_V/E(B-V) = 3.1$ ) obtained from the NASA/IPAC Extragalactic Database<sup>5</sup> in the direction of Hydra I. We fitted the emission lines with a Gaussian function and derived the line strength by computing the area under the best-fitting profile. The uncertainties were estimated by propagating the standard deviations of the Gaussian fit parameters. We extracted the emission line ratios [O III]/ $H\beta$  and [S II]/ $H\alpha$  from the 1D stacked spectrum and from four different regions across the galaxy extension, co-spatial with the major emission peaks of  $H\alpha$  and with radius equal to 1 arcsec (Fig. 6). In Fig. 7 we show the BPT diagram for UDG 6 1  $R_{\text{eff}}$ -stacked spectrum (in red) and for the other analysed regions (in black). The obtained values confirmed that UDG 6 hosts several star-forming regions.

### 4.4. Gas properties

The amplitude of gas emission lines can give us additional information on the nature of ionised gas and on the star formation activity in UDG 6. Before computing some useful emission line ratios, we estimated the galaxy internal extinction in V band ( $A_V$ ) by computing the Balmer decrement and adopting the Calzetti et al. (2000) attenuation law as implemented in Domínguez et al. (2013):

$$A_V = (4.05 \pm 0.80) \times 1.97 \log_{10} \left[ \frac{[H\alpha/H\beta]}{2.86} \right].$$

We obtained a value of  $A_V = 1.2 \pm 0.5$  mag. The uncertainty on the reddening and all derived quantities are estimated via the error propagation standard formula. We further computed the electron density parameter ( $n_e$ ), which gives us hints on the compactness of star-forming regions. To this aim, we measured the flux ratio of [S II] lines ( $R$ ) and adopted the relation described in Proxauf et al. (2014):

$$\log_{10}(n_e) = 0.0543 \tan(-3.0553R + 2.8506) + 6.98 - 10.6905R + 9.9186R^2 - 3.5442R^3, \quad (1)$$

The relation provided in Proxauf et al. (2014) presents a convenient polynomial fit description to the classic statistical equilibrium equations and has been widely applied for H II diagnostics at low redshift. We thus obtained  $\log_{10}(n_e) = 2.2 \pm 0.3 \text{ cm}^{-3}$ .

We estimated the gas metallicity following the calibration described in Dopita et al. (2016), based on the N2S2H $\alpha$  line ratio. This calibration is valid in the electron density range  $100 \leq n_e \leq 400 \text{ cm}^{-3}$  and our value falls within this range ( $n_e \approx 160 \text{ cm}^{-3}$ ). The relation has also been successfully applied by Lara-López et al. 2022 on a sample of star-forming galaxies in the Fornax cluster. We obtained  $12 + \log_{10}(\text{O}/\text{H}) = 7.7 \pm 0.2$  dex.

Finally, we estimated the star formation rate (SFR) by computing:  $\text{SFR} [M_{\odot}/\text{yr}] = 7.9 \times 10^{-42} L_{\alpha}$  (Kennicutt 1998). The parameter  $L_{\alpha}$  corresponds to the intrinsic luminosity of  $H\alpha$  corrected for dust extinction. We obtained a value for the SFR in UDG 6 of  $(1.9 \pm 0.1) \cdot 10^{-3} M_{\odot} \text{ yr}^{-1}$  and for the specific SFR of  $\text{sSFR} = \text{SFR}/M_{*} = (7 \pm 3) \cdot 10^{-11} \text{ yr}^{-1}$ . In the estimation of the SFR, we did not explicitly account for a possible obscured star formation component, despite the high dust content of the galaxy. To investigate this, we computed the  $V-R$  colour map by extracting broadband images from the MUSE data-cube. If highly dust-obscured star-forming regions are present, we expect to detect significantly redder colours and strong variations across the map. Instead, we find that the colours are of the order of 0.1 mag and show no significant spatial variation ( $\Delta(V-R) \sim 0.01$  mag). Moreover,  $H\alpha$  emission is broadly detected across the full extent of UDG 6. The absence of spatially localised regions with anomalously red colours without  $H\alpha$  detection argues against the presence of a significant amount of obscured star-forming regions.

We finally obtained an estimate of the mass of the ionised gas ( $M_{\text{gas}} = (9 \pm 2) \cdot 10^6 M_{\odot}$ ) following the prescription in Calabrò et al. (2017). The final fraction of ionised gas mass over the total baryonic one ( $M_{\text{b}} = M_{\text{gas}} + M_{*}$ ) is  $f_{\text{gas}} = M_{\text{gas}}/M_{\text{b}} = 0.24 \pm 0.08$ . We did not consider any other contribution of neutral hydrogen in the gas mass budget. Despite Hydra I having been covered by the WALLABY@ASKAP survey (Westmeier et al. 2022), the HI mass sensitivity at  $5\sigma$  allows for the detection of  $M_{\text{HI}} \geq 10^8 M_{\odot}$ .

<sup>5</sup> <https://ui.adsabs.harvard.edu/>

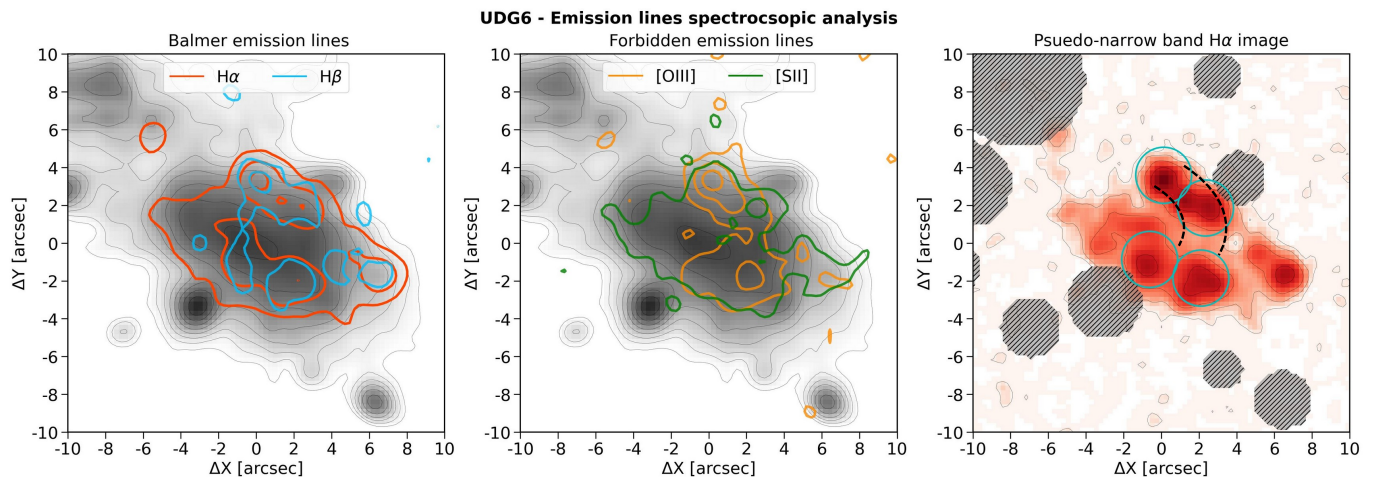


Fig. 6: Emission lines analysis of UDG 6. Left panel: the MUSE reconstructed image (grey) superimposed with contours of  $H\alpha$  and  $H\beta$  maps in red and blue, respectively. Central panel: the MUSE reconstructed image (grey) superimposed with contours of  $[O\text{ III}]$  and  $[S\text{ II}]$  maps in yellow and green, respectively. The contours of the MUSE image and the emission lines maps are convolved with a Gaussian kernel of size  $1 \times 1 \text{ pixel}^2$ . Right panel: pseudo-narrow band of  $H\alpha$  image. Grey hatched circles represent the masked regions, the cyan circles identify the apertures, and the black dashed line delimits the spiral-like feature.

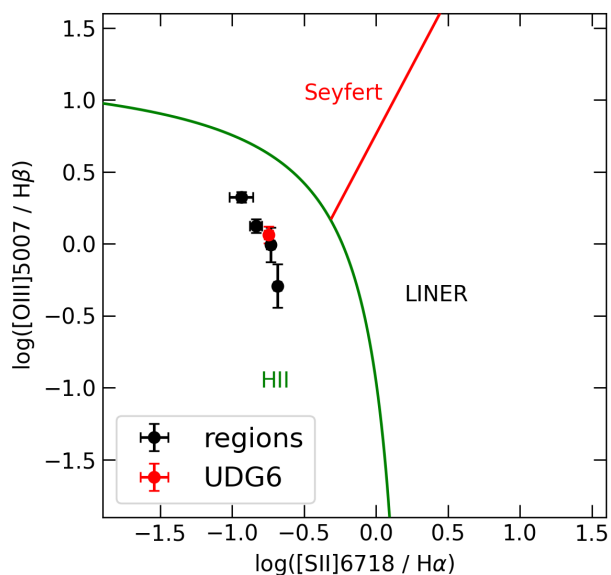


Fig. 7: BPT diagram (Baldwin et al. 1981). The red circle is the value for UDG 6 obtained from  $1R_{\text{eff}}$  stacked spectrum, while the black circles mark the values obtained from the four apertures. The green and red lines separate the regions of the AGN galaxy, the LINER objects, and the ionised regions, respectively.

We therefore cannot exclude the presence of HI mass lower than this limit in UDG 6. All of the previously stated quantities are extracted from the  $1R_{\text{eff}}$ -stacked spectrum, representing thus a lower limit.

#### 4.5. Gas velocity field

We extracted spatially resolved kinematic information of the ionised gas in UDG 6 following the same strategy described in Paper II. We started masking all the stars, background, and foreground sources in the FOV of the UDG, and we applied an adaptive Voronoi tessellation algorithm (Cappellari & Copin 2003) to bin the data and obtain a specific S/N per bin. The estimator of

the S/N adopted in Paper II has been applied to derive the average S/N of spectra dominated by absorption lines and with a smooth stellar continuum. The UDG 6's spectra contain instead strong emission lines for which the previously adopted estimator would not provide an accurate estimate of the S/N. For this reason, we additionally considered a dedicated line-based S/N estimator together with the S/N of the continuum.

The S/N is defined as the minimum of the continuum S/N and the quadratic sum of the S/Ns of each detected emission line, to ensure a robust estimate of the S/N across various spectral configurations. The signal of the line is estimated by integrating the flux of the continuum-subtracted emission line, while the noise is measured as the root mean square of the flux in two adjacent regions bracketing the line emission. The S/N of the continuum is evaluated locally in the same symmetrical regions around each line. Once the new S/N estimator is included in the algorithm, we applied the Voronoi binning on UDG 6's data-cube with a threshold of  $S/N = 10$ . This results in 10 independent bins with good-quality spectra ( $S/N \sim 12 - 14$ ).

We fitted each binned spectrum with the pPXF algorithm following a similar strategy for the 1D stacked spectrum as described in Section 4.1, with the only difference that instead of applying a specific spectral mask to each bin, we filtered the noisier regions by applying a 2 sigma-clipping. We extracted the gas kinematics by combining Balmer and forbidden lines into a single component, since, when taken as a single one, the Balmer and forbidden lines do not show evidence of different kinematics. The uncertainties were estimated by using the same Monte Carlo approach described in Section 4.1, by generating perturbations of the original spectrum and by repeating the spectral fitting. These uncertainties reflect the precision of the spectral fitting algorithm in the recovery of the fitted parameters, given the data quality. These statistical uncertainties range between  $0.5\text{--}2 \text{ km s}^{-1}$ .

In Fig. 8, we show S/N map of the Voronoi bins (left panel), the velocity field of the gas (central panel) and the velocity profile extracted along the galaxy's axes (right panel). The velocity profiles along the major axis shows a clear gradient in velocity. The amplitude of the rotation curve is roughly  $V_{\text{LOS}} \sim 14 \text{ km s}^{-1}$ . Assuming a galaxy inclination of  $i = \arccos(1 - \epsilon) = 66^\circ$ ,

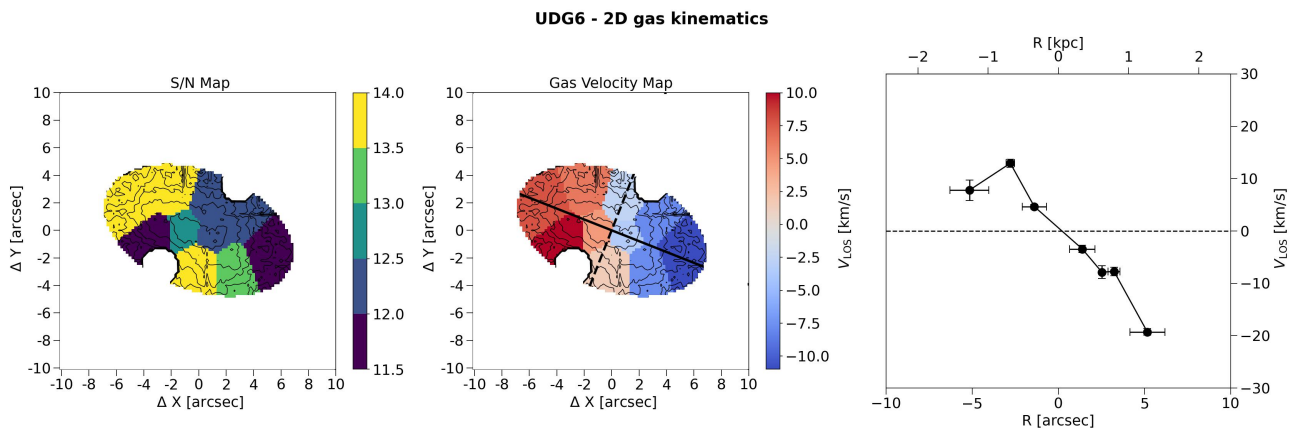


Fig. 8: Spatially-resolved gas kinematics of UDG 6. Left panel: Voronoi-binned map of the S/N. Central panel: ionised gas velocity map subtracted from the systemic velocity  $V_{\text{sys}}$ . The black solid and dashed lines mark the photometric major and minor axes of UDG 6, respectively. Right panel: velocity profile extracted along the galaxy’s major axis. The radial distance  $R$  is shown in projected angular (arcsec) and physical (kpc) distance.

we obtained a deprojected maximum velocity of  $V_{\text{max,depr}} = V_{\text{max}} / \sin(i) = 22 \text{ km s}^{-1}$  along the galaxy’s major axis. The peak velocity of UDG 6 occurs at  $\sim 1.3 R_{\text{eff}}$ , corresponding to the radius where the maximum rotation velocity is expected for a pure exponential disk ( $\sim 2.2 R_d$  with  $R_d$  the disk scale length) assuming  $R_{\text{eff}} \sim 1.7 R_d$  (Freeman 1970).

#### 4.6. Analysis of GCs

The identification of GCs associated with UDG 6 was carried out following the methodology introduced in Mirabile et al. (2026), which integrates MUSE spectroscopy with deep wide-field optical and near-infrared imaging from OmegaCAM@VST and VIRCAM@VISTA. From the analysis of the spectra of all compact sources in the field of UDG 6, we did not find the presence of any bound GC or intra-cluster GC. To inspect the population of faint GCs, for which the spectral S/N is too low ( $S/N \leq 2.5 \text{ \AA}^{-1}$ ), we exploited the wide wavelength coverage of the MUSE cube to create three images approximately equivalent to the SDSS  $g$ ,  $r$ ,  $i$  bands, which are then analysed together with the deep VIRCAM  $H$ -band observations of the cluster. We obtained photometric and morphometric information for all sources in the  $1' \times 1'$  field around UDG 6 and selected GC candidates based on their shape, colour-colour properties, and magnitudes ( $m_H \geq 22 \text{ mag}$ ). The resulting photometric catalogue is contaminated by Milky Way stars and faint background galaxies. We therefore first removed all sources spectroscopically identified as stars, background galaxies, or emission-line objects. The residual contamination was then treated using a statistical background decontamination technique (D’Abrusco et al. 2016; Cantiello et al. 2020; Mirabile et al. 2024). First, we characterised the contaminant population by analysing regions in an annulus between 15 and 30 arcsec from the galaxy centre, to determine the level of local background contamination. On-galaxy GC candidates were instead selected within  $1.5 R_{\text{eff}}$ . The number of GCs was then estimated as the difference between the on-galaxy GC-candidate density and the off-galaxy background density multiplied for the area within  $1.5 R_{\text{eff}}$ , corrected for the completeness of our data. The result of this analysis indicates that UDG 6 hosts no significant GC overdensity; the value ( $N_{\text{GC}} = 0.2 \pm 5.4$ ) is consistent with zero within uncertainties (Mirabile et al. in prep.).

## 5. Summary and discussion

In this Section, we briefly summarise the results obtained from the analysis carried out from the MUSE IF spectroscopy of UDG 6 and their physical implications. Table 2 reports the gas and stellar properties of UDG 6 derived in this work.

- Morphology: the isophotal analysis showed that UDG 6 is characterised by an elongated structure with coherent orientation projected on the sky plane (Section 3.1). The unsharp mask analysis revealed an arc-like structure on the west side of the main body of the galaxy (Section 3.2).

- Spectroscopic analysis: the UDG 6’s spectrum is characterised by the presence of strong emission line of ionised gas, such as Balmer ( $H\alpha$ ,  $H\beta$ ) and forbidden ( $[\text{O III}]$ ,  $[\text{N II}]$ ,  $[\text{S II}]$ ) lines, and extremely faint absorption features, such as  $H\beta$ , MgI and iron lines. The spectral fitting analysis on the  $1R_{\text{eff}}$ -stacked spectrum revealed the co-spatial presence of a gas and stellar component, ensuring that the gas is not merely projected along the line of sight. Due to the lack of strong absorption features, it was not possible to constrain the  $\sigma_{\text{LOS,*}}$  of the stellar component (Section 4.1).

- Stellar populations: the lack of strong absorption lines prevented us from obtaining a tight constraint on the age and metallicity of the stellar component (Section 4.2). The spectral fitting revealed a persistent old stellar component ( $\geq 3 \text{ Gyr}$ ). Unfortunately, we cannot constrain the stellar metallicity in UDG 6 via spectral fitting.

- Emission line source: we recovered the nature of ionisation and spatial distribution of the gas emission in UDG 6 (Section 4.3). We found that  $H\alpha$  is the most abundant component and, together with  $[\text{S II}]$ , is widely distributed across the whole galaxy’s extension. The distributions of the  $H\beta$  and  $[\text{O III}]$  emissions appeared instead more clumpy and patchy. From the analysis of the BPT diagram, we confirmed that UDG 6 is characterised by recent star-formation activity.

- Gas properties: UDG 6 is characterised by a significant dust content ( $A_V \sim 1.2 \text{ mag}$ ), diffuse star-forming regions ( $\log_{10}(n_e) \sim 2 \text{ cm}^{-3}$ ) and a significant metal-poor ( $12 + \log_{10}(\text{O}/\text{H}) = 7.7 \text{ dex}$ ) ionised gas amount. The extremely low value for SFR suggests that the star formation is inefficient or has been recently triggered (Section 4.4). The ionised gas fraction enclosed in  $1 R_{\text{eff}}$  is  $f_{\text{gas}} = 0.24 \pm 0.08$ .

Table 2: Stellar and gas properties of UDG 6.

Property		UDG 6
(1)	$M_{*,H}$	$[10^8 M_{\odot}]$ $0.18 \pm 0.07$
(2)	$V_{\text{LOS,gas}}$	$[\text{km s}^{-1}]$ $3559 \pm 1$
(3)	$V_{\text{LOS,*}}$	$[\text{km s}^{-1}]$ $3584 \pm 15$
(4)	$\sigma_{\text{LOS,Balmer}}$	$[\text{km s}^{-1}]$ $18 \pm 1$
(5)	$\sigma_{\text{LOS,Forbidden}}$	$[\text{km s}^{-1}]$ $22 \pm 4$
(6)	$12 + \log_{10}(\text{O}/\text{H})$	$[\text{dex}]$ $7.7 \pm 0.2$
(7)	$[M/\text{H}]$	$[\text{dex}]$ $-1.4 \pm 0.2$
(8)	SFR	$[10^{-3} M_{\odot} \text{ yr}^{-1}]$ $1.9 \pm 0.1$
(9)	sSFR	$[10^{-11} \text{ yr}^{-1}]$ $7 \pm 3$
(10)	$M_{\text{gas}}$	$[10^6 M_{\odot}]$ $9 \pm 2$
(11)	$f_{\text{gas}}$	$0.24 \pm 0.08$

**Notes.** Properties of UDG 6. (1): stellar mass derived from  $H$ -band image. (2-5): stellar and gas kinematics derived from  $1 R_{\text{eff}}$ -stacked spectrum. (6): gas metallicity. (7) stellar metallicity, derived by converting the gas metallicity with the prescription in [Fraser-McKelvie et al. \(2022\)](#). (8-9): star-formation rate and specific star-formation rate (10-11) ionised gas mass and mass fraction enclosed in an aperture of  $1 R_{\text{eff}}$ .

- Gas velocity field: we retrieved the gas velocity field of UDG 6 and extracted the rotation curve along the major photometric axis of the galaxy. UDG 6 shows clear hints of coherent rotation: Along the galaxy’s major axis, the velocity curve reaches a maximum value of  $V_{\text{max,depr}} = 22 \text{ km s}^{-1}$  on the deprojected galaxy plane (Section 4.5).

- GCs populations: the number of GCs in UDG 6 is consistent with zero ( $N_{\text{GC}} = 0.2 \pm 5.4$ , Section 4.6).

Taking all these elements together, we can conclude that UDG 6 shows evidence of an arc-like underlying structure, possibly related to the ionised gas and due to an external perturbation. UDG 6 seems to have an old underlying stellar component, but its precise age and metallicity cannot be strongly constrained. UDG 6 hosts a significant dust content and ionised gas amount with low metallicity and a coherent velocity field that slowly rotates. The ongoing star-formation activity in the galaxy appears bursty and diffuse in its whole extension. In the following sections, we consider the global properties of UDG 6 in relation to its location in the cluster and compare them with similar cases in the literature.

### 5.1. Is UDG 6 a peculiar galaxy in Hydra I?

The projected systemic velocity of UDG 6 ( $V_{\text{LOS,*}} = 3584 \pm 15 \text{ km s}^{-1}$ ) is consistent with the  $1\sigma_{\text{Hydra}}$  velocity distribution of the cluster ( $V_{\text{Hydra}} = 3683 \pm 46 \text{ km s}^{-1}$ , [Christlein & Zabludoff 2003](#)) where  $\sigma_{\text{Hydra}} = 724 \pm 31 \text{ km s}^{-1}$ , ([Lima-Dias et al. 2021](#)). We can thus confirm that UDG 6 is a cluster member of Hydra I, as the majority of the LEWIS sample ([Paper II](#)). According to its relative position and velocity in the projected phase-space diagram ([Forbes et al. 2023](#); [Buttitta et al. 2025](#)), UDG 6 is located in the early infall region (Fig. 9). This region contains the ancient infallers, i.e. galaxies that entered the cluster at earlier epochs and are now virialised with the system. There exists, however, the chance that galaxies classified as early infallers are instead interlopers ( $\sim 10\%$ ) or late infallers ( $\sim 15\%$ ) due to projection effects ([Rhee et al. 2017](#)).

In Hydra I, UDG 6 is located in the Northern overdensity of the cluster ([La Marca et al. 2022a](#)). This region is characterised by strong evidence of galaxy interactions and by the presence of intra-cluster light ([Spavone et al. 2024](#)). UDG 6 lies at

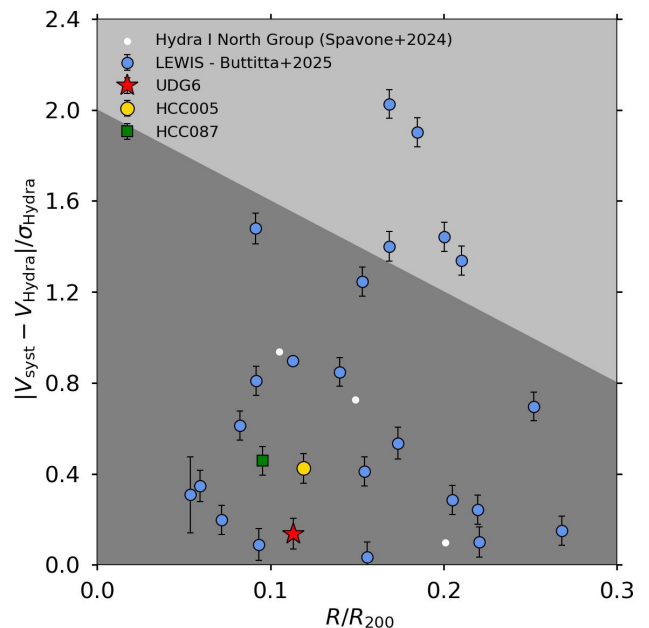


Fig. 9: Projected phase-space diagram for galaxies in Hydra I. The galaxy’s systemic velocity relative to the average velocity of the cluster, normalised by the cluster velocity dispersion ( $|V_{\text{syst}} - V_{\text{Hydra}}|/\sigma_{\text{Hydra}}$ ) is shown as a function of the projected clustercentric distance normalised by the cluster’s virial radius ( $R/R_{200}$ ). The dark and light grey regions represent the very early and the late infall regions, respectively. White and light blue dots represent the galaxies located in the North overdensity ([Spavone et al. 2024](#)) and the LEWIS sample ([Buttitta et al. 2025](#)), respectively. The red star, yellow circle, and green square symbols show the position of UDG 6, lenticular galaxy HCC 005, and the disrupted dwarf galaxy HCC 087, respectively.

a projected distance of 1.87 arcmin from the lenticular bright galaxy HCC 005, which corresponds to a projected separation of  $\sim 27 \text{ kpc}$  (see Fig. 1). The relative velocity between HCC 005 ( $V_{\text{syst}} = 3370 \pm 8 \text{ km s}^{-1}$ ) and UDG 6 is  $\Delta V \sim 190 \text{ km s}^{-1}$ . HCC 005 shows two prominent tails, evidence of some environmental perturbation acting on the galaxy. Nearby HCC 005, in the south-eastern direction, is located a tidally disrupted dwarf galaxy with a peculiar S-shape, HCC 087 ([Misgeld et al. 2008](#); [Koch et al. 2012](#)), a clear example of on-going interaction. All the discussed cases suggest that the environment might also have an impact on the structure of UDG 6, inducing the formation of the arc-like structure and triggered clumpy star-formation activity. A similar spiral-like structure has been reported in [Mancera Piña et al. \(2024\)](#), in a HI gas-rich UDG. However, there are important differences between them. UDG 6 shows an asymmetric single-armed feature, whereas the galaxy presented by [Mancera Piña et al. \(2024\)](#) appears symmetric and has a global disk-like spiral structure. Moreover, the two galaxies reside in different environments: UDG 6 is located in the inner region of a cluster, whereas AGC 114905 is found in an isolated/low-density environment. The asymmetric morphology of UDG 6, combined with its location in the cluster and proximity to HCC 005, supports an external origin, whereas the spiral structure in AGC 114905 is consistent with internal disk processes in a gas-rich system.

The majority of the LEWIS galaxies ( $\sim 75\%$ ) are located in very early infall region ([Paper II](#)), which includes UDGs with a broad range of properties in terms of stellar kinematics, metal-

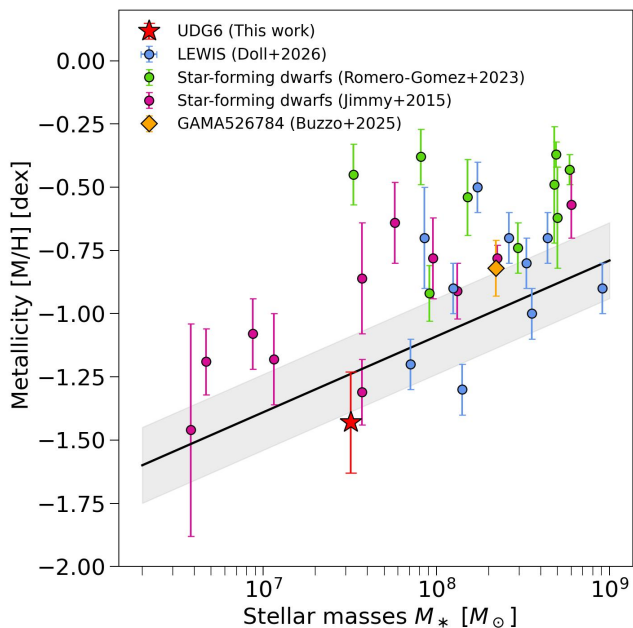


Fig. 10: Mass-Metallicity relation. The black solid line and shaded region correspond to the mass-metallicity relation for dwarfs and  $1\sigma$  uncertainties (Kirby et al. 2013). UDG 6 is represented by the red star; its stellar metallicity was derived by converting the gas-phase measurement using the prescription in Fraser-McKelvie et al. (2022). The LEWIS sample is marked with light blue dots (Doll et al. 2026). We additionally reported the value for GAMA 526784 (Buzzo et al. 2025) (orange diamond) and those for the samples of star-forming dwarf galaxies studied by Jimmy et al. 2015 (magenta) and Romero-Gómez et al. 2023 (green).

licity, and star formation history (Paper II and Paper V). The UDGs of the LEWIS sample, similarly to typical UDGs in other clusters, are red, gas-poor, and quenched, with dwarf-like or slightly higher metallicity. Most of these properties, constrained by the analysis of the stellar component, cannot be compared with UDG 6’s properties, because we do not have reliable results. In contrast, UDG 6 seems to retain a significant amount of gas reservoir and presents hints of ongoing star formation activity. UDG 6 may represent a rare example of a UDG located in the virialised region of the cluster with evidence of ionised gas, or be an interloper which is starting to feel the cluster forces, thus leaving an unperturbed gas velocity field.

### 5.2. A star-forming UDG in a cluster: a rare UDG or a transition phase?

Despite a consistent number of gas-rich UDGs having been studied through HI data, UDGs with strong signatures of ionised gas are rare. Recently, Khim et al. (2025) have discovered an unusual UDG with a coherent stellar velocity field, several GCs and star-forming knots characterised by clear  $H\beta$ ,  $[O\text{II}]$  and  $[O\text{III}]$  emission lines. Similarly, Buzzo et al. (2025) combined HST and Subaru/HSC imaging data with IF spectroscopy from MUSE, to fully characterise a GC-rich star-forming UDG, where strong emission lines, such as Balmer lines ( $H\alpha$  and  $H\beta$ ) and forbidden lines of  $[N\text{II}]$ ,  $[S\text{II}]$  and  $[O\text{III}]$ , are detected, and a coherent stellar and ionised gas velocity field is derived. However, these UDGs are located in low-density environments.

Kadowaki et al. (2017) reported the serendipitous discovery in the Coma Cluster of a UDG with evidence of ionised gas, characterised by  $[N\text{II}]$ ,  $[O\text{III}]$  and Balmer emission lines. Junais et al. (2021) presented a detailed multi-wavelength analysis of a HI gas-rich UDG in the Virgo Cluster. Nearby this UDG, ionised-gas knots have been detected in the same HI cloud associated with the UDG, suggesting that the latter has undergone some ram-pressure stripping event, which removed HI gas clouds from it and subsequently triggered star-formation in clumpy knots. These UDGs, similarly to UDG 6, are dominated by an old underlying stellar population. Their rarity suggests that the detection of ionised gas in cluster UDGs could be a transient phenomenon, quickly quenched by the dense environment. Recently, Taylor et al. (2026) reported the discovery of a gas-rich UDG in the Virgo cluster whose HI content has been displaced by ram-pressure stripping as the galaxy enters the cluster for the first time. Similar to UDG 6, this system has suffered from environmental processes. Environmental processes may also have affected the formation and evolution of the Hydra I UDG 32, which Hartke et al. (2025) propose to have formed from pre-processed material originating from the south-east group.

UDG 6 hosts a significant dust content and it is characterised by an inefficient star-formation activity with a SFR of  $\sim 2 \cdot 10^{-3} M_{\odot}/\text{yr}$ . Kado-Fong et al. (2022) retrieved the SFRs of a sample of 22 nearby HI rich UDGs located in low-density environments. Their estimates rely on an Kroupa (2001) IMF, providing thus systematically lower values than those obtained with a Salpeter (1955) IMF, and were obtained from SED fitting including UV data, thus tracing different star formation timescales. We convert the value of UDG 6’s SFR, to be comparable with the value obtained by Kado-Fong et al. 2022 ( $\text{SFR}_{\text{Kroupa}} \approx \text{SFR}_{\text{Salpeter}}/1.5$ ), obtaining an even lower value ( $\text{SFR} \sim 1.3 \cdot 10^{-3} M_{\odot}/\text{yr}$ ). On average, the SFR values of the analysed sample are higher ( $\text{SFR} \sim 10^{-2} - 10^{-1} M_{\odot}/\text{yr}$ ) than the estimate retrieved for UDG 6, with the only exception of the field UDG AGC 219200, which shows a SFR comparable with UDG 6’s measure. Slightly lower values have been reported in star-forming dwarfs ( $\sim 1.7 \cdot 10^{-4} M_{\odot}/\text{yr}$ , Lee et al. 2009), whereas higher estimates have been found for field gas-rich LSB galaxies ( $2 \cdot 10^{-2} M_{\odot}/\text{yr}$ , Greco et al. 2018). Despite being somewhat consistent with literature values, the extremely low value of SFR can alternatively be explained by the stochasticity of the initial mass function (Boselli et al. 2023), i.e. a discontinuous sampling of stellar mass distribution that can strongly bias the inferred SFR value. Finally, UDG 6 hosts a discrete ionised gas content within its effective radius ( $f_{\text{gas}} = 0.24 \pm 0.2$ ), characterised by a low gas metallicity ( $12 + \log_{10}(\text{O}/\text{H}) = 7.7 \pm 0.2$  dex). Since we were not able to constrain the metallicity of the stellar component from spectral fitting, we adopted the conversion proposed in Fraser-McKelvie et al. (2022) to obtain the stellar metallicity and compare it with similar studies. We therefore obtained  $[M/H] = -1.43 \pm 0.2$  dex. Given its low stellar mass with respect to the other galaxies in LEWIS, UDG 6 has the lowest metallicity of the sample, and it is consistent within  $1\sigma$  with the Kirby et al. 2013 relation (Fig. 10). Its metallicity is also consistent with the value of star-forming dwarf galaxies even down to stellar masses of  $M_{*} \sim 10^{6.6} M_{\odot}$  (Jimmy et al. 2015).

### 5.3. On the formation channel of UDG 6

Considering all the quantities obtained from spectroscopic analysis, we review the various formation scenarios proposed for

UDGs with a discrete gas amount by attempting to identify the most suitable for UDG 6. Gas-rich UDGs might originate from ‘puffed-up dwarfs’, whose stellar distribution is stretched to larger radii, while retaining significant amounts of gas. The involved mechanisms could be either internal or external. High-spin DM halos or frequent episodes of star-formation feedback push the gas from the galaxy’s centre to the outskirts, thus transforming a dwarf galaxy into a diffuse system and suppressing the star-formation activity (Amorisco & Loeb 2016; Rong et al. 2017; Di Cintio et al. 2017). Alternatively, UDGs with a moderate-to-low amount of gas can originate from weak gravitational interaction and galaxy mergers, which can inflate dwarf galaxies into UDG-like systems (Bennet et al. 2018; Müller et al. 2019). Gas-rich UDGs might form from collisional debris from galaxy mergers or close encounters (Lelli et al. 2015; Duc et al. 2014; Ploekinger et al. 2018; Ivleva et al. 2024) or from gas clumps from ram-pressure stripped galaxies infalling into the clusters (Poggianti et al. 2017; Grishin et al. 2021).

Despite not being precisely constrained in age and metallicity, UDG 6 shows evidence of an old underlying stellar population. The distribution of stars and ionised gas is nearly co-spatial and almost uniformly distributed in the galaxy’s extension. In addition, the low-metallicity gas coherently rotates within the galaxy. These features indicate that the star formation activity has been suppressed, preventing the enrichment of the gas and supporting the idea that UDG 6 has evolved as a normal dwarf galaxy with a significant amount of gas before becoming diffuse. Together with the morphological structure and coherent gas rotation, UDG 6’s properties disfavour the scenario in which UDGs form via internal mechanisms, which tends to remove all the gas from the innermost region of the galaxy. We can further exclude the ram-pressure stripping scenario, since the UDGs originated with this mechanism would have an irregular morphology and a dominant young stellar component.

A reasonable evolutionary path for UDG 6 seems to be the ‘puffed-up scenario’, similarly to the other UDGs in the LEWIS sample (Paper V), but due to external processes. A strong interaction with the hot intra-cluster medium would have stripped the gas from UDG 6, strongly altering its coherent rotation. Most probably a weak tidal interaction with nearby massive galaxies as proposed by Bennet et al. (2018) can originate UDG-like system with properties similar to UDG 6. A mild environmental perturbation from the cluster, possibly due to the dynamically active region where UDG 6 resides, may have contributed to triggering only recently a clumpy star-formation activity that we observed today. This would justify the extremely low value for SFR and the unperturbed gas with a coherent rotation.

## 6. Conclusions

We presented a detailed spectroscopic analysis of a gas-rich UDG in the Hydra I cluster, identified within the LEWIS project, showing clear evidence of diffuse star-forming regions. This galaxy is the only object in our sample exhibiting strong emission lines in the MUSE data cube. For UDG 6, we constrained the properties of the ionised gas, including its morphology, kinematics, and metallicity. However, the age and metallicity of the stellar component remain poorly constrained; we can only infer the presence of a metal poor old-to-intermediate-age stellar population. We argued that UDG 6 could be in a transient evolutionary phase, in which a quenched UDG, originating from a puffed-up dwarf via external mechanisms, can re-ignite localised star formation under environmental effects.

Further insight into the nature and evolutionary pathway of UDG 6 will require a multi-wavelength approach. Ultraviolet observations will help constrain the recent star formation rate, while deep HI data will probe the presence of neutral gas reservoirs, providing a critical test of the proposed scenario. In addition, combining multi-band photometry with spectral energy distribution (SED) fitting will enable more robust constraints on the underlying stellar populations. Retrieving an accurate stellar velocity dispersion will allow us to infer the DM content, a fundamental key parameter to disentangle the different proposed formation pathways for UDG 6. All these quantities will allow a comprehensive characterisation of this peculiar UDG and clarify the role of the environment in shaping its properties.

These efforts will also be essential for mapping the UDG population at larger cluster-centric distances. Using new deep imaging covering the Hydra I cluster out to the virial radius, we have already identified 24 new UDG candidates (Borsato et al., in prep.). Follow-up spectroscopic observations will improve the statistical characterisation of star-forming UDGs and their connection to the cluster environment.

*Acknowledgements.* We wish to thank the anonymous Referee whose comments helped us to improve the clarity of the manuscript. Based on observations collected at the European Southern Observatory under ESO programmes 108.222P.001, 108.222P.002, 108.222P.003. This work is based on the funding from the INAF through the GO large grant in 2022, to support the LEWIS data reduction and analysis (PI E. Iodice). The authors wish to thank P. Mancera Piña, O. Müller, E. Sola, and L. Coccatto for the useful comments and discussions on the work presented in this paper. J.H acknowledges support from TC-SMT through a starting grant. JF-B acknowledges support from the PID2022-140869NB-I00 grant from the Spanish Ministry of Science and Innovation. DF thanks the ARC for financial support via DP250101673. EMC recognises the support of the Italian Ministry of University and Research (MUR) grant PRIN 2022 2022383WFT “SUNRISE” (CUP C53D23000850006) and Padua University grants DOR 2023-2025.

## References

- Adams, E. A. K., Šiljeg, B., Ponomareva, A. A., et al. 2026, *A&A*, 708, A122  
 Amorisco, N. C. & Loeb, A. 2016, *MNRAS*, 459, L51  
 Arnaboldi, M., Ventimiglia, G., Iodice, E., Gerhard, O., & Coccatto, L. 2012, *A&A*, 545, A37  
 Bacon, R., Accardo, M., Adjali, L., et al. 2010, in *Proc. SPIE*, Vol. 7735, Ground-based and Airborne Instrumentation for Astronomy III, 773508  
 Bacon, R., Conseil, S., Mary, D., et al. 2017, *A&A*, 608, A1  
 Baldwin, J. A., Phillips, M. M., & Terlevich, R. 1981, *PASP*, 93, 5  
 Bennet, P., Sand, D. J., Zaritsky, D., et al. 2018, *ApJ*, 866, L11  
 Blakeslee, J. P., Vazdekis, A., & Ajhar, E. A. 2001, *MNRAS*, 320, 193  
 Boselli, A., Fossati, M., Côté, P., et al. 2023, *A&A*, 675, A123  
 Bradley, L., Sipőcz, B., Robitaille, T., et al. 2023, *astropy/photutils: 1.8.0*  
 Buttitta, C., Iodice, E., Doll, G., et al. 2025, *A&A*, 694, A276  
 Buzzo, M. L., Forbes, D. A., Jarrett, T. H., et al. 2024, *MNRAS*, 529, 3210  
 Buzzo, M. L., Zanella, A., Hilker, M., et al. 2025, *A&A*, 700, A165  
 Calabrò, A., Amorín, R., Fontana, A., et al. 2017, *A&A*, 601, A95  
 Calzetti, D., Armus, L., Bohlin, R. C., et al. 2000, *ApJ*, 533, 682  
 Cantiello, M., Venhola, A., Grado, A., et al. 2020, *A&A*, 639, A136  
 Cappacioli, M., Spavone, M., Grado, A., et al. 2015, *A&A*, 581, A10  
 Cappellari, M. 2017, *MNRAS*, 466, 798  
 Cappellari, M. 2023, *MNRAS*, 526, 3273  
 Cappellari, M. & Copin, Y. 2003, *MNRAS*, 342, 345  
 Cappellari, M. & Emsellem, E. 2004, *PASP*, 116, 138  
 Christlein, D. & Zabludoff, A. I. 2003, *ApJ*, 591, 764  
 D’Abrusco, R., Cantiello, M., Paolillo, M., et al. 2016, *ApJ*, 819, L31  
 Di Cintio, A., Brook, C. B., Dutton, A. A., et al. 2017, *MNRAS*, 466, L1  
 Doll, G., Buttitta, C., Iodice, E., et al. 2026, *A&A*, 707, A88  
 Domínguez, A., Siana, B., Henry, A. L., et al. 2013, *ApJ*, 763, 145  
 Dopita, M. A., Kewley, L. J., Sutherland, R. S., & Nicholls, D. C. 2016, *Ap&SS*, 361, 61  
 Duc, P.-A., Paudel, S., McDermid, R. M., et al. 2014, *MNRAS*, 440, 1458  
 Ferré-Mateu, A., Gannon, J. S., Forbes, D. A., et al. 2023, *MNRAS*  
 Fitzpatrick, E. L. & Massa, D. 2007, *ApJ*, 663, 320  
 Forbes, D. A., Gannon, J., Iodice, E., et al. 2023, *MNRAS*, 525, L93  
 Fraser-McKelvie, A., Cortese, L., Groves, B., et al. 2022, *MNRAS*, 510, 320

- Freeman, K. C. 1970, *ApJ*, 160, 811
- Freudling, W., Romaniello, M., Bramich, D. M., et al. 2013, *A&A*, 559, A96
- Gannon, J. S., Ferré-Mateu, A., & Forbes, D. A. 2026, *PASA*, 43, e031
- Gannon, J. S., Forbes, D. A., Romanowsky, A. J., et al. 2022, *MNRAS*, 510, 946
- Gault, L., Leisman, L., Adams, E. A. K., et al. 2021, *ApJ*, 909, 19
- Gerhard, O. E. 1993, *MNRAS*, 265, 213
- Girardi, L., Bressan, A., Bertelli, G., & Chiosi, C. 2000, *Astron. Astrophys. Suppl. Ser.*, 141, 371
- Greco, J. P., Greene, J. E., Strauss, M. A., et al. 2018, *ApJ*, 857, 104
- Grishin, K. A., Chilingarian, I. V., Afanasiev, A. V., et al. 2021, *Nature Astronomy*, 5, 1308
- Hartke, J., Iodice, E., Gullieuszik, M., et al. 2025, *A&A*, 695, A91
- Hess, K. M., Kotulla, R., Chen, H., et al. 2022, *A&A*, 668, A184
- Hinshaw, G., Larson, D., Komatsu, E., et al. 2013, *ApJS*, 208, 19
- Into, T. & Portinari, L. 2013, *MNRAS*, 430, 2715
- Iodice, E., Cantiello, M., Hilker, M., et al. 2020, *A&A*, 642, A48
- Iodice, E., Hilker, M., Doll, G., et al. 2023, *A&A*, 679, A69
- Iodice, E., Spavone, M., Capaccioli, M., et al. 2021, *The Messenger*, 183, 25
- Ivleva, A., Remus, R.-S., Valenzuela, L. M., & Dolag, K. 2024, *A&A*, 687, A105
- Janowiecki, S., Jones, M. G., Leisman, L., & Webb, A. 2019, *MNRAS*, 490, 566
- Jimmy, Tran, K.-V., Saintonge, A., et al. 2015, *ApJ*, 812, 98
- Jonais, Boissier, S., Boselli, A., et al. 2021, *A&A*, 650, A99
- Kado-Fong, E., Greene, J. E., Huang, S., & Goulding, A. 2022, *ApJ*, 941, 11
- Kadowaki, J., Zaritsky, D., & Donnerstein, R. L. 2017, *ApJ*, 838, L21
- Karunakaran, A., Spekkens, K., Zaritsky, D., et al. 2020, *ApJ*, 902, 39
- Kennicutt, Jr., R. C. 1998, *ARA&A*, 36, 189
- Khim, D. J., Zaritsky, D., Sandoval Ascencio, L., Cooper, M. C., & Donnerstein, R. 2025, *ApJ*, 989, 154
- Kirby, E. N., Cohen, J. G., Guhathakurta, P., et al. 2013, *ApJ*, 779, 102
- Koch, A., Burkert, A., Rich, R. M., et al. 2012, *ApJ*, 755, L13
- Kroupa, P. 2001, *MNRAS*, 322, 231
- La Marca, A., Iodice, E., Cantiello, M., et al. 2022a, *A&A*, 665, A105
- La Marca, A., Peletier, R., Iodice, E., et al. 2022b, *A&A*, 659, A92
- Lara-López, M. A., Galán-de Anta, P. M., Sarzi, M., et al. 2022, *A&A*, 660, A105
- Lee, M. G., Yuk, I.-S., Park, H. S., Harris, J., & Zaritsky, D. 2009, *ApJ*, 703, 692
- Leisman, L., Haynes, M. P., Janowiecki, S., et al. 2017, *ApJ*, 842, 133
- Lelli, F., Duc, P.-A., Brinks, E., et al. 2015, *A&A*, 584, A113
- Lim, S., Côté, P., Peng, E. W., et al. 2020, *ApJ*, 899, 69
- Lima-Dias, C., Monachesi, A., Torres-Flores, S., et al. 2021, *MNRAS*, 500, 1323
- Makda, N. A., Blyth, S. L., & Skelton, R. E. 2025, *MNRAS*, 544, 3824
- Mancera Piña, P. E., Aguerrí, J. A. L., Peletier, R. F., et al. 2019, *MNRAS*, 485, 1036
- Mancera Piña, P. E., Fraternali, F., Oman, K. A., et al. 2020, *MNRAS*, 495, 3636
- Mancera Piña, P. E., Golini, G., Trujillo, I., & Montes, M. 2024, *A&A*, 689, A344
- Mancera Piña, P. E., Peletier, R. F., Aguerrí, J. A. L., et al. 2018, *MNRAS*, 481, 4381
- Marleau, F. R., Cuillandre, J.-C., Cantiello, M., et al. 2025, *A&A*, 697, A12
- Mirabile, M., Cantiello, M., Lonare, P., et al. 2024, *A&A*, 691, A104
- Mirabile, M., Cantiello, M., Rejkuba, M., et al. 2026, *A&A*, 705, A117
- Misgeld, I., Mieske, S., & Hilker, M. 2008, *A&A*, 486, 697
- Müller, O., Rich, R. M., Román, J., et al. 2019, *A&A*, 624, L6
- Osterbrock, D. E. & Ferland, G. J. 2006, *Astrophysics of gaseous nebulae and active galactic nuclei* (University Science Books)
- Papastergis, E., Adams, E. A. K., & Romanowsky, A. J. 2017, *A&A*, 601, L10
- Ploeckinger, S., Sharma, K., Schaye, J., et al. 2018, *MNRAS*, 474, 580
- Poggianti, B. M., Moretti, A., Gullieuszik, M., et al. 2017, *ApJ*, 844, 48
- Prole, D. J., van der Burg, R. F. J., Hilker, M., & Davies, J. I. 2019, *MNRAS*, 488, 2143
- Proxauf, B., Öttl, S., & Kimeswenger, S. 2014, *A&A*, 561, A10
- Rhee, J., Smith, R., Choi, H., et al. 2017, *ApJ*, 843, 128
- Román, J. & Trujillo, I. 2017, *MNRAS*, 468, 4039
- Romero-Gómez, J., Peletier, R. F., Aguerrí, J. A. L., et al. 2023, *MNRAS*, 522, 130
- Rong, Y., Guo, Q., Gao, L., et al. 2017, *MNRAS*, 470, 4231
- Safarzadeh, M. & Scannapieco, E. 2017, *ApJ*, 850, 99
- Sales, L. V., Navarro, J. F., Peñafiel, L., et al. 2020, *MNRAS*, 494, 1848
- Salpeter, E. E. 1955, *ApJ*, 121, 161
- Soto, K. T., Lilly, S. J., Bacon, R., Richard, J., & Conseil, S. 2016, *MNRAS*, 458, 3210
- Spavone, M., Iodice, E., Lohmann, F. S., et al. 2024, *A&A*, 689, A306
- Spekkens, K. & Karunakaran, A. 2018, *ApJ*, 855, 28
- Taylor, R., Partík, V., & Minchin, R. 2026, *A&A*, 707, A107
- Trujillo, I., Roman, J., Filho, M., & Sánchez Almeida, J. 2017, *ApJ*, 836, 191
- van der Burg, R. F. J., Muzzin, A., & Hoekstra, H. 2016, *A&A*, 590, A20
- van der Marel, R. P. & Franx, M. 1993, *ApJ*, 407, 525
- van Dokkum, P. G., Romanowsky, A. J., Abraham, R., et al. 2015, *ApJ*, 804, L26
- Vazdekis, A., Casuso, E., Peletier, R. F., & Beckman, J. E. 1996, *ApJS*, 106, 307
- Vazdekis, A., Koleva, M., Ricciardelli, E., Röck, B., & Falcón-Barroso, J. 2016, *MNRAS*, 463, 3409
- Vazdekis, A., Ricciardelli, E., Cenarro, A. J., et al. 2012, *MNRAS*, 424, 157
- Venhola, A., Peletier, R., Laurikainen, E., et al. 2017, *A&A*, 608, A142
- Weilbacher, P. M., Palsa, R., Streicher, O., et al. 2020, *A&A*, 641, A28
- Westmeier, T., Deg, N., Spekkens, K., et al. 2022, *PASA*, 39, e058
- Wittmann, C., Lisker, T., Ambachew Tilahun, L., et al. 2017, *MNRAS*, 470, 1512
- Zaritsky, D. & Behroozi, P. 2023, *MNRAS*, 519, 871
- Zaritsky, D., Donnerstein, R., Dey, A., et al. 2023, *ApJS*, 267, 27

<sup>1</sup> INAF – Astronomical Observatory of Capodimonte, Salita Moiarriello 16, I-80131, Naples, Italy

<sup>2</sup> University of Naples “Federico II”, C.U. Monte Sant’Angelo, Via Cinthia, 80126, Naples, Italy

<sup>3</sup> INAF – Osservatorio Astronomico di Padova, Vicolo dell’Osservatorio 5, I-35122 Padova, Italy

<sup>4</sup> Armagh Observatory and Planetarium, College Hill, Armagh, BT61 9DG UK

<sup>5</sup> INAF – Astronomical Observatory of Abruzzo, Via Maggini, 64100, Teramo, Italy

<sup>6</sup> Gran Sasso Science Institute, viale Francesco Crispi 7, I-67100 L’Aquila, Italy

<sup>7</sup> Finnish Centre for Astronomy with ESO, (FINCA), University of Turku, FI-20014 Turku, Finland

<sup>8</sup> Tuorla Observatory, Department of Physics and Astronomy, University of Turku, FI-20014 Turku, Finland

<sup>9</sup> Turku Collegium for Science, Medicine and Technology (TCSMT), University of Turku, FI-20014 Turku, Finland

<sup>10</sup> European Southern Observatory, Karl-Schwarzschild-Strasse 2, 85748 Garching bei München, Germany

<sup>11</sup> INAF – Astronomical Observatory of Abruzzo, Via Maggini, 64100, Teramo, Italy

<sup>12</sup> Dipartimento di Fisica e Astronomia “G. Galilei”, Università di Padova, vicolo dell’Osservatorio 3, I-35122 Padova, Italy

<sup>13</sup> Institute of Astronomy, University of Cambridge, Madingley Road, Cambridge CB3 0HA, UK

<sup>14</sup> Instituto de Astrofísica de Canarias, Calle Vía Láctea s/n, 38200 La Laguna, Spain

<sup>15</sup> Departamento de Astrofísica, Universidad de La Laguna, E-38200, La Laguna, Tenerife, Spain

<sup>16</sup> Centre for Astrophysics & Supercomputing, Swinburne University of Technology, Hawthorn VIC 3122, Australia

<sup>17</sup> European Space Agency/ESTEC, Keplerlaan 1, 2201 AZ Noordwijk, The Netherlands

<sup>18</sup> Leiden Observatory, Leiden University, PO Box 9513, NL-2300 RA Leiden, The Netherlands

<sup>19</sup> European Southern Observatory, Alonso de Cordova 3107, Vitacura, Santiago, Chile

<sup>20</sup> Sub-Dep. of Astrophysics, Dep. of Physics, University of Oxford, Denys Wilkinson Building, Keble Road, Oxford OX1 3RH, United Kingdom